Battery Energy

WILEY

RESEARCH ARTICLE OPEN ACCESS

Confined-Assembled FeNi Alloy-Embedded Porous Carbon Nanosheet Reactors as Efficient Bifunctional Electrocatalysts for Rechargeable Zinc-Air Batteries

Yafeng Li[1,2,3] | Yannan Xia[1,3] | Rui Wang[1,3,4] | Ren Luo[1] | Zihan Meng[2] | Shuyu Chen[1,2,3] | Jiaqi Shuai[1,2,3] | Hao Li[5,6] | Haolin Tang[1,2,3]

[1]State Key Laboratory of Advanced Technology for Materials Synthesis and Processing, Wuhan University of Technology, Wuhan, China | [2]National Energy Key Laboratory for new hydrogen-ammonia energy technologies, Foshan Xianhu Laboratory, Foshan, People's Republic of China | [3]Hubei Key Laboratory of Fuel Cells, Wuhan University of Technology, Wuhan, China | [4]School of Chemistry, Chemical Engineering and Life Science, Wuhan University of Technology, Wuhan, China | [5]Helmholtz Institute Ulm (HIU), Ulm, Germany | [6]Institute of Nanotechnology, Karlsruhe Institute of Technology (KIT), Karlsruhe, Germany

Correspondence: Rui Wang (rwang@whut.edu.cn) | Hao Li (hao.li2@kit.edu) | Haolin Tang (thln@whut.edu.cn)

Received: 25 February 2026 | **Revised:** 11 April 2026 | **Accepted:** 15 April 2026

Funding: Basic and Applied Basic Research Foundation of Guangdong Province, Grant/Award Number: 2024B1515130002; Foshan Xianhu Laboratory of the Advanced Energy Science and Technology Guangdong Laboratory, Grant/Award Numbers: XHD2024-23000000-05, XHD2025-422501-01; National Natural Science Foundation of China, Grant/Award Number: 52506222; Fundamental Research Funds for the Central Universities, Grant/Award Number: WUT. 104972025ZHZXhp0013

Keywords: carbon nanotubes | porous carbon nanosheets | self-assembly | zinc-air battery | ZnO template

ABSTRACT

Highly dispersed metallic active centers supported on two-dimensional conductive carbon materials hold great promise for energy-conversion applications; however, their structurally controllable synthesis remains challenging. Herein, we propose a template-assisted assembly strategy using ZnO as a structure-directing template to construct a branched porous carbon framework embedded with FeNi alloy species. Unlike conventional hard templates that merely create pores, the ZnO template creates a favorable microenvironment for CNT growth and simultaneously generates abundant mesopores upon its removal. Through coordination interactions between folic acid and Fe/Ni ions, two-dimensional confined precursors are first formed. This branched architecture, conceptually described as a porous carbon reactor, integrates a high specific surface area, efficient electron/ion transport pathways, and densely distributed catalytic active sites. As a result, the optimized catalyst exhibits excellent bifunctional ORR/OER activity in alkaline media, with a small potential gap ($\Delta E = 0.67$ V). The assembled rechargeable zinc-air battery delivers a high peak power density of 239 mW cm^{-2} together with outstanding cycling stability (over 200 h). This work provides a new paradigm for designing noble-metal-free electrocatalysts through template-guided assembly.

1 | Introduction

Driven by global efforts toward climate-change mitigation and carbon neutrality, the development of efficient and sustainable energy-conversion and storage technologies has become increasingly important [1–7]. Among emerging electrochemical energy systems, rechargeable zinc-air batteries (ZABs) are considered one of the most promising candidates for next-generation power devices because of their high theoretical energy density, environmental benignity, and the natural

Yafeng Li and Yannan Xia contributed equally to this study.

abundance of zinc resources [8–11]. However, the sluggish kinetics of the oxygen reduction reaction (ORR) during discharge and the oxygen evolution reaction (OER) during charge severely limit the power output and cycling durability of ZABs [12–15]. Therefore, the development of highly active and durable noble-metal-free bifunctional electrocatalysts remains a key challenge for the practical commercialization of ZABs [9, 16–18].

Transition-metal (e.g., Fe, Co, and Ni) and nitrogen co-doped carbon materials have attracted extensive attention for oxygen electrocatalysis because of their tunable electronic structure, abundant active centers, and high electrical conductivity [12, 19–22]. In particular, atomically dispersed metal-nitrogen (M-N_x) sites can maximize metal utilization and provide high intrinsic catalytic activity [20, 23]. Nevertheless, isolated metal sites are susceptible to aggregation during high-temperature treatment, and their adsorption energies toward multiple oxygen intermediates are often difficult to optimize simultaneously. To address these limitations, constructing multicomponent catalysts that combine atomically dispersed sites with metal/alloy nanoparticles has been demonstrated to be an effective strategy, as the synergistic interactions between different active species can enhance bifunctional ORR/OER performance [24, 25]. In this context, developing two-dimensional conductive carbon substrates with highly exposed active interfaces is particularly desirable, yet the precise and controllable synthesis of such architectures remains challenging [26].

Self-assembly provides a versatile route for regulating micro-/nanostructures with high precision [27]. Folic acid, which contains multiple coordination sites and exhibits assembly-induced structural organization, is an attractive molecular building block for constructing ordered precursors [28, 29]. Meanwhile, hard-template methods remain among the most effective approaches for introducing hierarchical porosity into carbon-based catalysts, as comprehensively reviewed in recent literature [30–36]. For instance, the nanoemulsion modular assembly method has emerged as a scalable, efficient, and versatile platform for synthesizing functional mesoporous nanomaterials, surpassing traditional templating methods in the controllability of pore size, structure, and morphology [37]. Additionally, the versatility of ZnO-based templating has been demonstrated to extend beyond carbon matrices to various transition metal systems, including Fe, Co, Ni, Cu, and even noble metals such as PtCo alloys, enabling gram-scale production of atomically dispersed metal catalysts [38–40]. Therefore, integrating self-assembly with hard-template engineering offers a promising pathway to simultaneously tailor catalyst composition, morphology, and pore structure, thereby optimizing mass/electron transport and catalytic performance.

In this work, we report a template-assisted assembly strategy to fabricate a FeNi alloy-embedded porous carbon nanoreactor for bifunctional oxygen electrocatalysis, using ZnO as a structure-directing and sacrificial template (Figure 1a). Critically, unlike previous reports where ZnO is used merely as a pore former, our ZnO template plays a dual structure-directing function: it creates a favorable microenvironment for the in-situ growth of carbon nanotubes and, upon removal, generates abundant mesopores [41–43]. It should be noted that the actual catalytic growth of CNTs is primarily driven by FeNi alloy nanoparticles formed in situ via the Vapor–Liquid–Solid (VLS) mechanism, while the ZnO template mainly provides a spatially confined and defect-rich environment for CNT nucleation [44–48]. Folic acid serves as the carbon/nitrogen precursor and coordinates with Fe and Ni ions to form two-dimensional confined precursors during hydrothermal treatment, while ZnO nanoparticles are uniformly incorporated into the precursor matrix [49–51]. This process leads to a branched conductive network composed of interwoven carbon nanotubes and porous carbon nanosheets, with highly dispersed FeNi active centers embedded in the N-doped carbon framework. The key conceptual advance lies in the integration of molecular self-assembly with a removable ZnO template to construct a hierarchical structure—conceptually described as a "porous carbon reactor"—that synergistically combines high surface area, efficient mass/electron transport, and abundant FeNi/M-N_x active sites in a single material [52]. Owing to this unique architecture, the resulting catalyst exhibits outstanding bifunctional ORR/OER activity and enables high-performance rechargeable ZABs with prolonged cycling stability (over 200 h). It provides a practical strategy for the structural engineering of advanced noble-metal-free electrocatalysts.

2 | Results and Discussion

2.1 | Characterization of Porous Carbon Nanoreactor

Scanning electron microscopy (SEM) analysis clearly reveals the regulatory function performed by the ZnO template over the microstructure of the material (Figure 1b–d and Supporting Information S1: Figure S1). FeNiP-900 (FeNiN/porous carbon nanosheets pyrolyzed at 900°C) sample without the template exhibits a typical two-dimensional nanosheet structure with only a few pores on its surface (Supporting Information S1: Figure S1a–c). In contrast, the FeNiCP (FeNiN/carbon nanotubes/porous carbon nanosheets) series materials obtained after adding the ZnO template all exhibited significant morphological evolution, forming a composite three-dimensional network where carbon nanosheets and carbon nanotubes are interwoven. This structural transformation can be traced to the role of ZnO as a catalyst for carbon nanotube growth in the pyrolysis process. Furthermore, ZnO particles embedded as physical barriers between the interlayers of the M-FA (M = Fe, Ni) precursor effectively suppressed excessive nanosheet growth, significantly reducing their size. This unique nanosheet/nanotube composite configuration offers multiple advantages: the hollow tubes of carbon nanotubes and the interfacial regions formed with nanosheets provide abundant catalytic active sites [53]. Concurrently, the tridimensional interconnection architecture possesses a combination of elevated volumetric surface coverage, excellent electrical connectivity, and structural flexibility [54]. This design effectively inhibits the agglomeration of metallic nanoparticles within the catalytic system, thereby significantly enhancing the available density of catalytically active centers and overall catalytic performance [55].

To investigate the fine microstructure of the materials in depth, a series of samples were additionally characterized via transmission electron microscopy (TEM) (Figure 1e,f). Referring to Supporting Information S1: Figure S2a, the FeNiP-900 sample without a template exhibits a typical thin-layer nanosheet

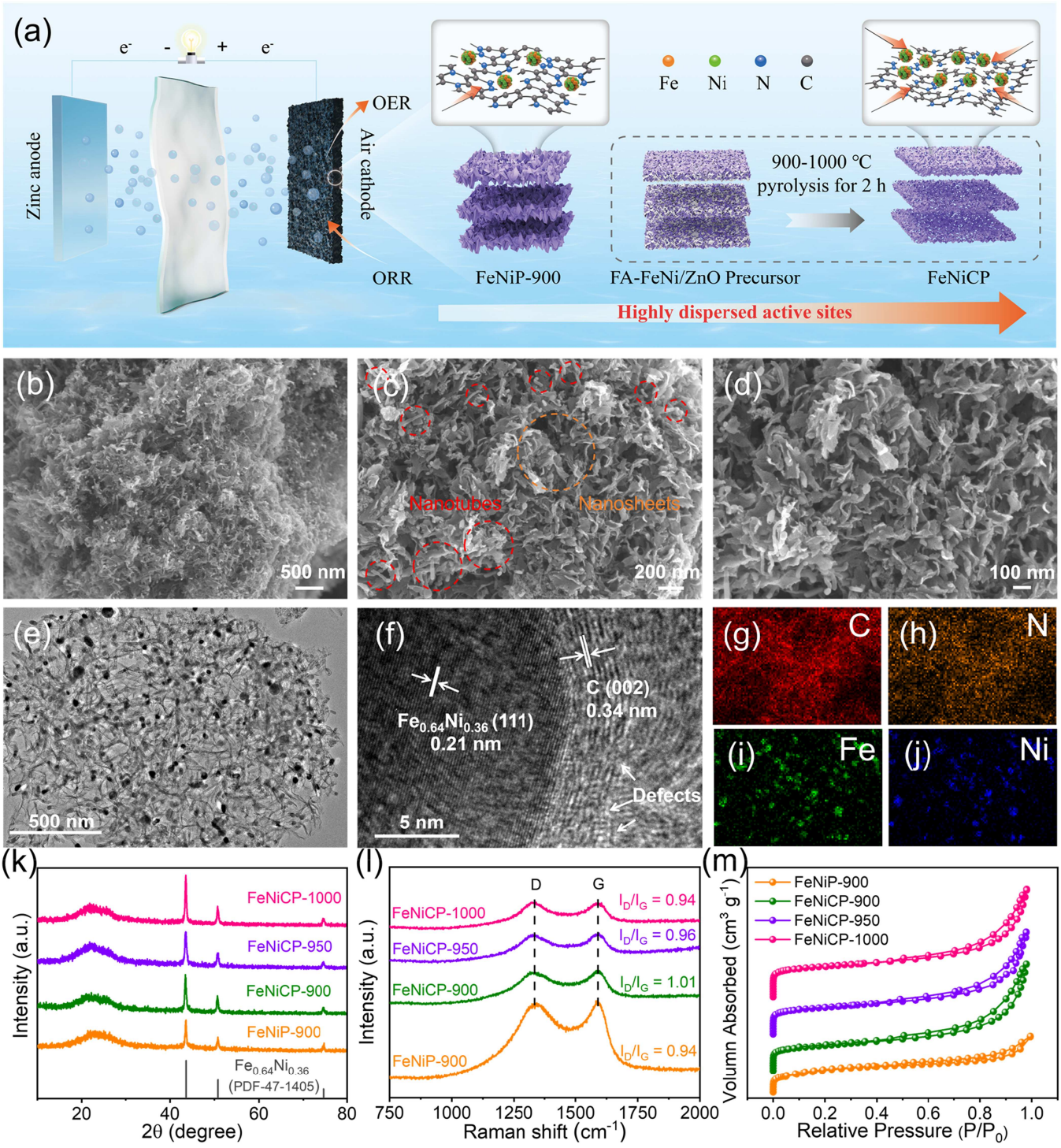

FIGURE 1 | (a) Schematic diagram of the FeNiCP preparation. SEM images of (b–d) FeNiCP-950, (e–f) TEM, and (g–j) HAADF-STEM elemental mapping of FeNiCP-950, (k) XRD patterns, (l) Raman spectra, (m) N_2 adsorption-desorption isotherms of FeNiP-900, FeNiCP-900, FeNiCP-950, and FeNiCP-1000.

morphology with metal particles distributed over a wide size range (15–200 nm). In stark contrast, the FeNiCP-900 sample obtained after introducing the ZnO template exhibits a composite three-dimensional structure where nanosheets are interwoven with carbon nanotubes (Supporting Information S1: Figure S2b). Crucially, the metal particle size in this sample was significantly reduced, indicating that the ZnO-induced composite structure effectively suppresses metal agglomeration during high-temperature processing. This suppression effect is most pronounced in FeNiCP-950, where the metal particle size is further diminished to 5–30 nm (Figure 1d). High-resolution TEM images (Figure 1f) clearly show prominent crystal lattice striations within these nanoparticles. The 0.21 nm interplanar spacing is characteristic of the (111) face-centered cubic plane in the FeNi-based alloy (PDF#47-1405), while the approximately 0.34 nm interlayer spacing at the particle periphery corresponds with the (002) hexagonal planar structure of graphite-type carbon. confirming the successful formation of a

core-shell structure (FeNi@C) [26]. To provide more representative structural evidence, we added a low-magnification TEM image (Supporting Information S1: Figures S3a and S4a) showing a wider field of view, and selected-area electron diffraction (SAED, Supporting Information S1: Figure S4b) revealed diffraction rings from graphitic carbon (002), FeNi alloy (111), (220), and (311), confirming the systematic coexistence of the carbon shell and alloy core. Statistical analysis of 40 randomly selected particles (Supporting Information S1: Figure S5) showed that 86% exhibited a clear core-shell structure with an average carbon shell thickness of 3–5 nm, indicating that this structure is the dominant morphological feature. The graphitized carbon shell in this structure effectively shields the internal metallic active center, enhancing its stability during electrochemical cycling. However, at a pyrolysis condition was elevated to 1000°C (Supporting Information S1: Figure S2c), the metal particle size increased again. This was attributed to metal atom migration and Ostwald ripening of the particles caused by the excessively high temperature [56].

Furthermore, combined elemental distribution mapping analysis (Figure 1g–j) indicates that C, N, Fe, and Ni are evenly dispersed across the material, confirming successful anchoring of the FeNi alloy within the nitrogen-doped carbon substrate. Thus, the microstructural features reveal at the nanoscale the critical role of the ZnO template in optimizing both the dispersion and stability of the active position.

The crystallographic structure of the catalyst was characterized by X-ray diffraction (XRD), depicted in the inset of Figure 1k. Widely diffracted peaks were observed around 26° for all specimens; this angle is characteristic of the carbon (002) plane, confirming the presence of a carbon-based matrix. Concurrently, characteristic diffraction peaks at 43.6°, 50.8°, and 74.7° correlate with the (111), (200), and (220) crystalline planes of $Fe_{0.64}Ni_{0.36}$, indicating successful incorporation of the FeNi alloy into the carbon framework [57]. To further confirm alloy formation and exclude phase separation, we performed a precise comparison of the experimentally measured XRD peak positions with those of pure Ni (PDF#04-0850). The (111) diffraction peak of FeNiCP-950 is located at 43.6°, whereas that of pure Ni is at 44.5°. This 0.9° shift toward lower angles clearly indicates lattice expansion caused by Fe atom solid solution, which is a well-established criterion for FeNi alloy formation (Supporting Information S1: Figure S6) [58–60]. As the pyrolysis temperature increased, the diffraction peaks of this alloy phase gradually become sharper, indicating enhanced crystallinity. Based on the XRD data, we calculated the lattice constant of FeNiCP-950 to be 3.595 Å (Supporting Information S1: Table S1), which closely matches the theoretical value of 3.592 Å for the $Fe_{0.64}Ni_{0.36}$ alloy, further confirming the successful formation of the expected solid-solution alloy. The degree of carbon framework defects in the material was quantified using Raman spectral analysis (Figure 1l). All samples exhibited distinctive peaks at around 1345 and 1580 cm^{-1}, representing disordered carbon atoms (D peak) and graphitized sp^2 carbon (G peak), respectfully [61] The I_D/I_G ratio (1.01) of the FeNiCP-900 sample with ZnO template was higher than that of FeNiP-900 without template (0.94), indicating that ZnO introduction induced more defects in the carbon skeleton, which is beneficial for optimizing catalytic activity.

Nitrogen adsorption-desorption testing was utilized to assess the porosity characteristics of the materials (Figure 1m). The adsorption isotherms of all samples exhibited a pronounced upward trend in the lower pressure range ($P/P_0 < 0.1$), indicative of abundant micropores. According to the IUPAC 2015 classification, the distinct hysteresis loops observed in the medium-to-high-pressure region ($0.4 < P/P_0 < 1.0$) were identified as H4-type, confirming the presence of mesopores originating from slit-shaped pores formed by the stacking of nanosheets as well as from the removal of ZnO templates [62]. As demonstrated by Supporting Information S1: Table S2, the bulk surface areas of FeNiCP-900 (381.6 $m^2 g^{-1}$) were significantly higher than those of FeNiP-900 (242.4 $m^2 g^{-1}$), directly attributable to the abundant mesoporous structure created after removing ZnO as the hard template. The porosity distribution (Supporting Information S1: Figure S7) further demonstrates that the sample incorporating ZnO exhibits a distinct mesoporous-microporous multi-level pore architecture, providing favorable conditions for substance transport during the reactive stages.

X-ray photoelectron spectra (XPS) are utilized to analyze the superficial composition of the material and its chemical states (Supporting Information S1: Figure S8a). Full-spectrum reveals that all samples contain C, N, O, and trace amounts of Fe and Ni, confirming the effective incorporation of FeNi species into the carbon matrix. Notably, no Zn 2p characteristic peak was detected in the spectra of the series of samples incorporating ZnO, indicating that the ZnO template was completely removed during pyrolysis. Peak fitting of the N 1 s spectrum (Figure 2a) assigns the signals to pyridine nitrogen (~398.5 eV), putative metal-nitrogen coordination (M-N_x, ~399.2 eV), pyrrole nitrogen (~400.1 eV), graphitic nitrogen (~401.1 eV), and nitric oxide (~403.0 eV) [63]. Quantitative analysis based on Supporting Information S1: Figure S8c and S9 indicates that the total content of pyridine nitrogen, putative M-N_x, pyrrole nitrogen, and graphitic nitrogen in FeNiCP-900 reaches 88.7%, significantly higher than the 83.0% observed in FeNiP-900, while FeNiCP-950 exhibits an even higher content of 89.6%, supporting Information S1: Table S3 details the nitrogen species content in the four catalysts. Among these, pyridine nitrogen and graphitic nitrogen are considered to effectively enhance ORR activity, while the putative M-N_x and pyrrole nitrogen serve as key catalytic centers for ORR and OER, respectively. Although the observed binding energy shifts suggest electronic coupling between the FeNi alloy and the N-doped carbon matrix, we note that XPS alone cannot determine the precise coordination geometry of M-N_x; direct structural confirmation would require additional techniques such as X-ray absorption spectroscopy [64, 65]. Additionally, the fitted features of 284.8, 285.7, and 287.2 eV within the C 1 s spectrum (Supporting Information S1: Figure S8c) correspond to C═C, C—N, and C═O bond vibrations, respectively. The existence of C—N peak directly validates the success of nitrogen doping.

Through in-depth analysis of the chemical species at material interfaces using X-ray photoelectron spectroscopy (XPS), the critical influence of the ZnO template on the nature of reactive species can be elucidated. The O 1 s spectrum (Supporting Information S1: Figure S8d) shows that the signal intensity attributed to the metal-oxygen bond (M–O) at ~530.0 eV is significantly weaker for FeNiCP-900 than for FeNiP-900, indicating lower oxidation of the surface FeNi alloy. This confirms the FeNi@C core-shell structure observed by TEM, where the outer graphite carbon layer effectively suppresses oxidation of the inner alloy core in air [66]. Concurrently, abundant

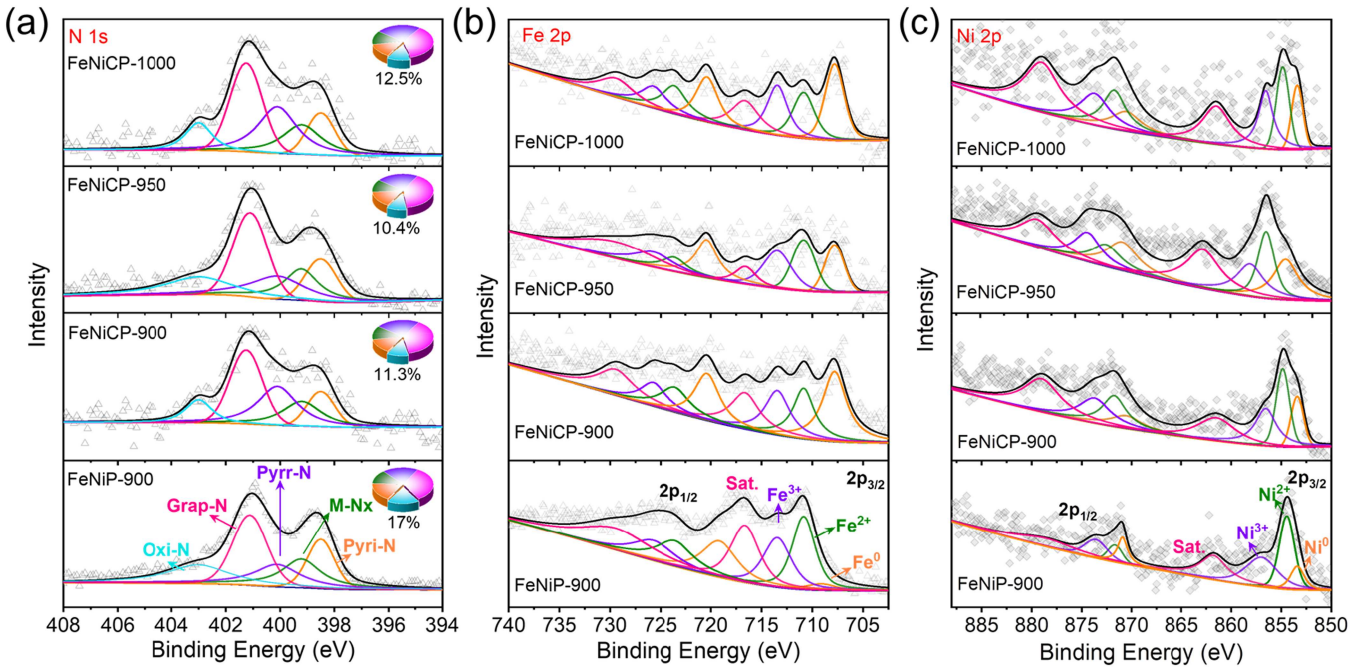

FIGURE 2 | (a) XPS N 1 s, (b) XPS Fe 2p, and (c) XPS Ni 2p spectra of all four samples.

surface hydroxyl and adsorbed water groups enhance hydrophilicity at the electrode/electrolyte interface, facilitating mass transfer during reactions [67].

Quantitative analysis of the Fe 2p (Figure 2b) and Ni 2p (Figure 2c) spectra provides further crucial evidence. The relative content of zero-valent metals (Fe^0, Ni^0) corresponding to the FeNi alloy in FeNiCP-900 is notably elevated compared with the template-free control sample. This directly confirms that the introduction of the ZnO template and the unique composite structure it induces can stabilize and enrich the FeNi alloy catalytic centers, which serve as the core catalytic sites within the catalyst. The remaining iron and nickel signals in ionic states primarily originate from putative metal-nitrogen coordination structures ($M\text{-}N_x$) and minor surface oxidation.

Based on the above characterization analysis, the multiple synergistic mechanisms of the ZnO template have been clearly revealed. During pyrolysis, ZnO creates a favorable microenvironment for the in-situ growth of carbon nanotubes (the actual catalytic sites are primarily provided by in-situ formed FeNi alloy nanoparticles via the VLS mechanism) and simultaneously serves as a sacrificial template, whose removal creates abundant mesoporous structures. Both processes collectively lead to the final product—a porous nitrogen-doped carbon nanosheet/carbon nanotube composite anchoring highly dispersed FeNi nanoparticles. This unique structure combines the benefits of large bulk surface area, exceptional conductivity, structural integrity, and effectively suppressing the agglomeration and loss of active metals. Consequently, it significantly enhances the available density of active sites and overall catalytic performance.

2.2 | Bifunctional ORR/OER Activity

To systematically assess oxygen reduction performance of the fabricated catalysts, rotating disc electrode measurements were conducted within a 0.1 M KOH electrolyte saturating in oxygen. As demonstrated in Figure 3a, introduction of the ZnO template significantly enhanced the ORR rate of the catalyst. The initial potential and half-cell voltage of FeNiCP-900 reached 0.96 and 0.86 V, outperforming the template-free FeNiP-900 (0.93 V, 0.80 V). Notably, FeNiCP-950, obtained via pyrolysis at 950°C, exhibited the most outstanding catalytic performance. Its overpotential reached 1.01 V and half-cell voltage was 0.89 V, exceeding those for conventional Pt/C catalyst (0.97 V, 0.85 V). These improvements are mainly due to the development of the most advanced carbon nanosheet/carbon nanotube composite network structure at this optimized temperature, which minimizes the size of metallic nanoclusters and exposes the highest density of reaction sites [68].

The catalytic kinetics were evaluated via Tafel curves (Figure 3b). FeNiCP-950 exhibited the smallest Tafel slope (60.4 mV dec^{-1}), significantly less than Pt/C (74.9 mV dec^{-1}), indicating accelerated ORR reaction kinetics. This conclusion is further supported by the electrochemical impedance analysis (Figure 3c), where the catalyst demonstrated the lowest charging resistance. This advantage stems from its hierarchical porous composite structure, which provides efficient pathways for both electron conduction and mass transfer [62, 69].

The longevity of a catalytic system is a crucial indicator for its practical application. Through chronoamperometry testing (Figure 3d), FeNiCP-950 maintained 88.4% of its original current efficiency after continuous service for 22 h. In contrast, Pt/C exhibited a current retention rate of only 74.2% after just 17 h under identical conditions. This outstanding stability stems from the protective role of the outer graphite carbon layer within the FeNi@C core-shell structure, which effectively prevents corrosion and loss of the internal core active components during electrochemical cycling [70]. FeNiCP-950 demonstrates superior comprehensive performance to conventional Pt/C in ORR reactivity, reaction kinetics, and long-term durability, highlighting its potential for application in energy conversion devices.

To elucidate the kinetic mechanism of the ORR on the catalyst, linear sweep voltammetry (LSV) curves were measured at various stirring speeds (Figure 4a–e) [71]. The electron transition number computed using the Koutecky–Levich equation is shown in Figure 4f. Notably, FeNiCP-950 exhibits an exceptionally impressive electron transition number of 3.99, approaching the theoretical value of 4.0. This indicates that its ORR process highly follows an efficient four-electron transfer pathway, further confirming its superior intrinsic catalytic activity [65]. This *n* value is consistent with RRDE-measured

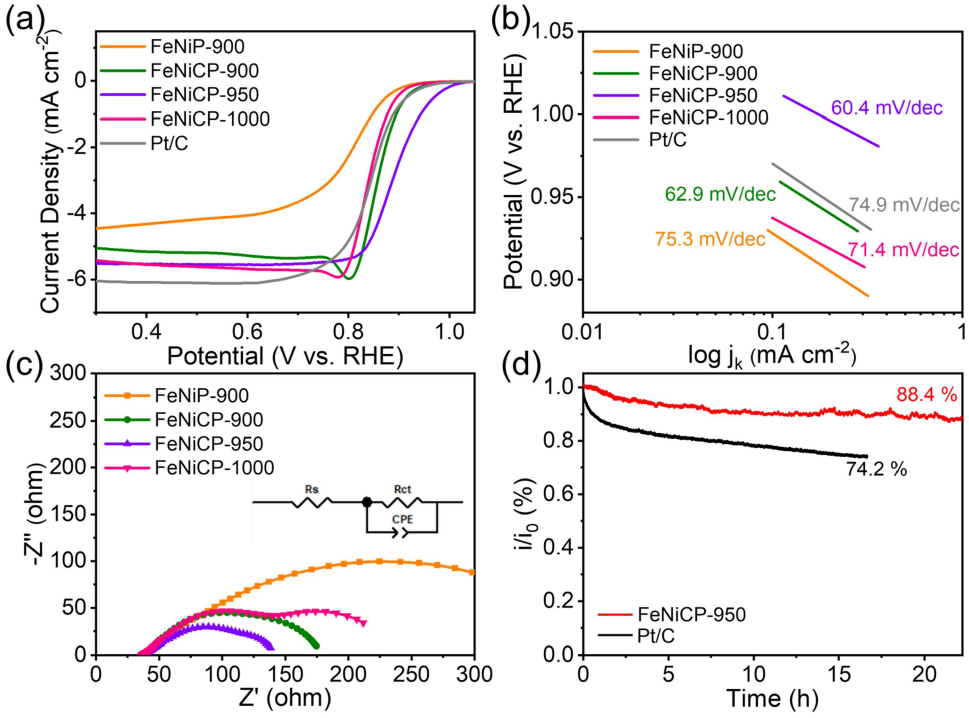

FIGURE 3 | (a) Linear sweep voltammetry, (b) corresponding Tafel plots, (c) Nyquist diagrams of all four samples for ORR in 0.1 M KOH. Inset: equivalent circuit with R_s, R_{ct}, and CPE. (d) chronoamperometric responses of FeNiCP-950 and Pt/C for ORR within 0.1 M KOH.

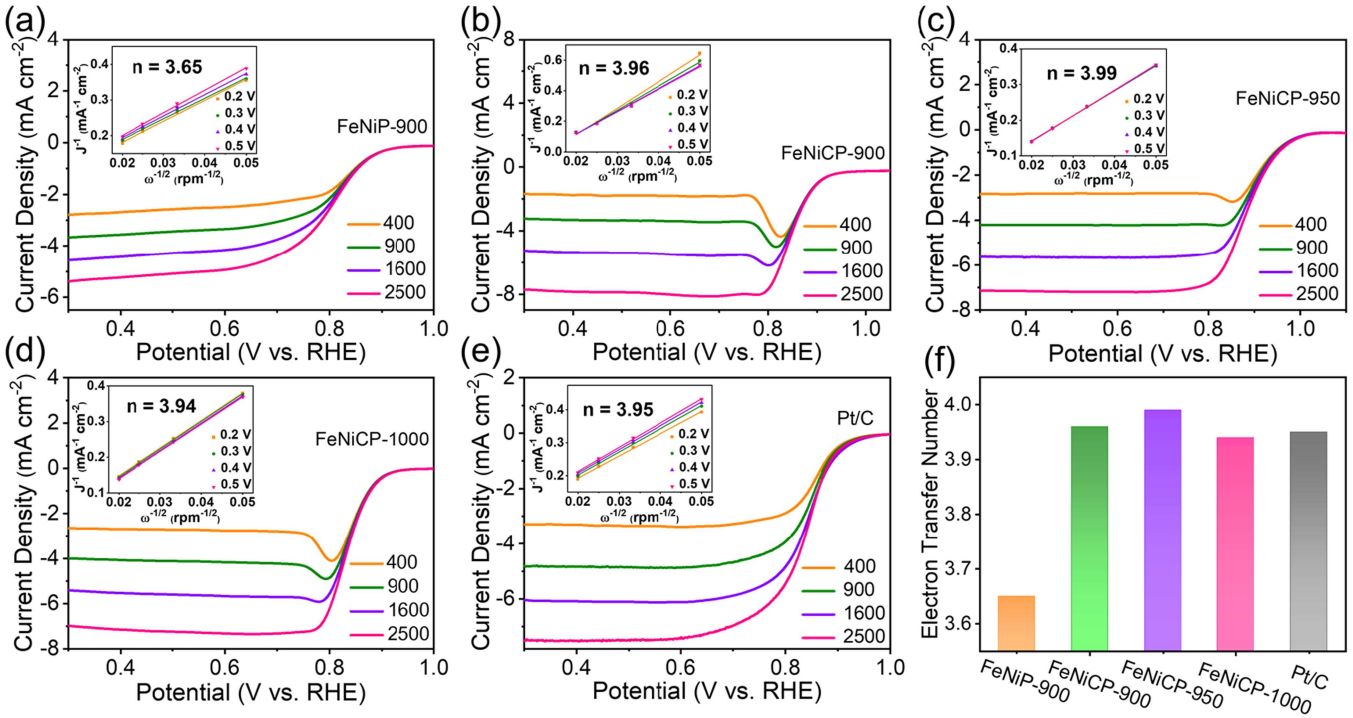

FIGURE 4 | (a) The LSV profiles of (a) FeNiP-900, (b) FeNiCP-900, (c) FeNiCP-950, (d) FeNiCP-1000 and (e) Pt/C at a sequence of rotation disc speeds, and the illustration shows the corresponding K–L curves at 0.3, 0.4, 0.5, 0.6 V along with the calculated electron transport number n. (f) Statistical diagram of electron transfer number calculated for all samples.

values (3.96–3.98) reported for similar FeNi-based catalysts in the literature (Supporting Information S1: Table S4).

By testing the cycling voltaic ampere diagram at various scan speeds (Supporting Information S1: Figure S10), the double-layer capacitance (C_{dl}) of the material was calculated to assess its electrochemical active surface area (ECSA). Supporting Information S1: Figure S11 demonstrates that FeNiCP-950 exhibits the highest C_{dl} value (28.4 mF cm^{-2}) [72]. This is primarily ascribed to its large specific surface area, abundant hierarchical porosity, resulting in a high density of exposed reactive species, all facilitated by its well-developed carbon nanosheet/carbon nanotube composite structure [73]. These factors collectively promote the progression of interfacial electrochemical reactions.

2.3 | Zinc-Air Battery Performance

To provide a more comprehensive assessment of the catalyst's overall performance, its OER activity was evaluated [72]. As shown in Figure 5a, the introduction of the ZnO template significantly reduced the OER overpotential operating at 10 mA cm^{-2}: this overpotential for FeNiCP-900 was 363 mV, significantly lower than that of FeNiP-900 without the template (500 mV). Among these, FeNiCP-950 exhibited the most outstanding OER reactivity, with a low activation overpotential of 334 mV, even outperforming commercial RuO_2 catalysts (355 mV). This exceptional activity stems from the material's unique porous composite structure, which provides it with a massive volumetric surface area, abundant transport channels, excellent thermal conductivity, and a densely packed network of FeNi active sites [65]. Dynamic reaction analysis further confirmed its advantages. As shown in Figure 5b, FeNiCP-950 exhibited the steepest Tafel slope (88.9 mV dec^{-1}), demonstrating the fastest OER reaction kinetics. Moreover, constant potential cycling tests (Figure 5c) reveal that FeNiCP-950 exhibits an overpotential increase of only 33 mV after 20 h of continuous operation, demonstrating significantly superior long-term stability compared with RuO_2. This stability is attributed to the Fe-Ni@C nucleolus structure, which effectively shields active sites from corrosion at elevated potentials. To further investigate possible surface reconstruction, we performed XPS analysis on the FeNiCP-950 electrode before and after OER (Supporting Information S1: Figure S12 and Table S5). The results show that the Ni^{3+}/Ni^{2+} ratio increased from 71.5% to 91.6%, and the Fe^{3+} signal slightly intensified after OER, consistent with literature reports on surface reconstruction of FeNi-based catalysts forming active (oxy)hydroxide phases under OER conditions [74–77]. The moderate increase in overpotential (33 mV) may reflect normal fluctuations during the dynamic equilibrium of Fe leaching, and is significantly smaller than the decay observed for RuO_2. To comprehensively evaluate the properties of ORR and OER, the bifunctional activation parameter ΔE (defined as the voltage drop between $E_j = 10$ and $E_{1/2}$) is typically employed [78]. As shown in Figure 5d, FeNiCP-950 exhibits the lowest ΔE (0.67 V), indicating its outstanding ORR/OER bifunctional catalytic activity in alkaline media. This performance establishes a solid foundation for its utilization as reusable ZABs and other energy devices.

We subsequently validated the practical application potential of FeNiCP-950 by assembling it within the air cathode catalyst of a liquid zinc-air battery. Figure 6 demonstrates this battery exhibits outstanding comprehensive performance: its open-circuit potential reaching as 1.49 V (Figure 6a) and demonstrates a narrow potential gap in the charge-discharge cyclic voltammetry curves (Figure 6b). At charge-discharge potential drops

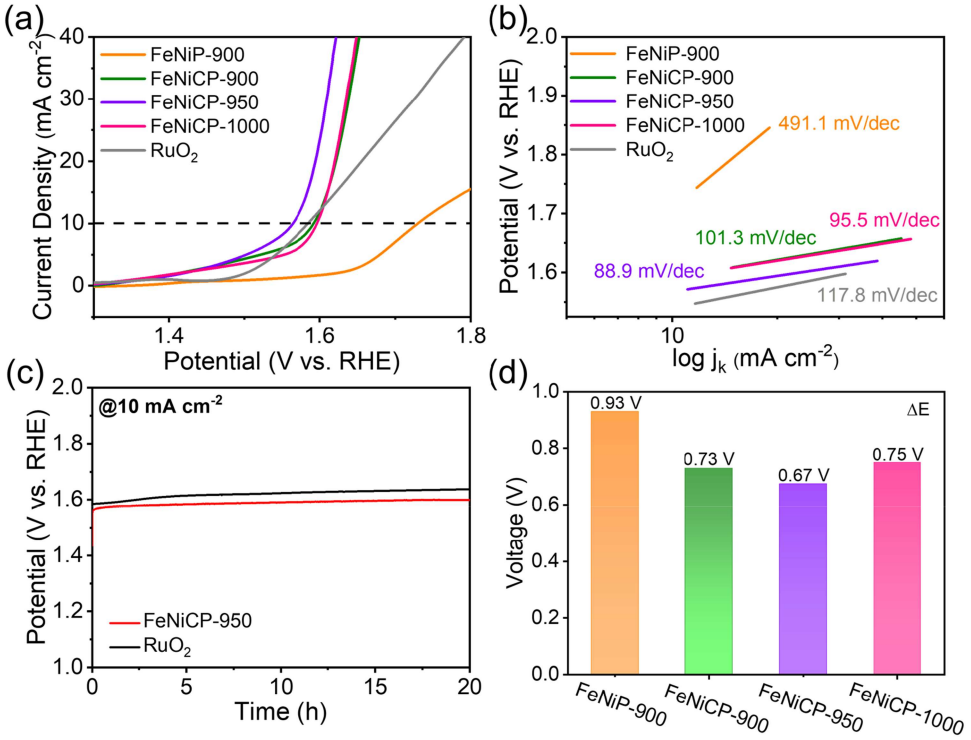

FIGURE 5 | (a) Linear sweep voltammetry, (b) corresponding Tafel slopes, (c) chronopotentiometry responses at the anode of FeNiCP-950 and RuO_2 for OER within 0.1 M KOH, (d) ORR/OER bifunctional catalytic performance for all four catalytic materials.

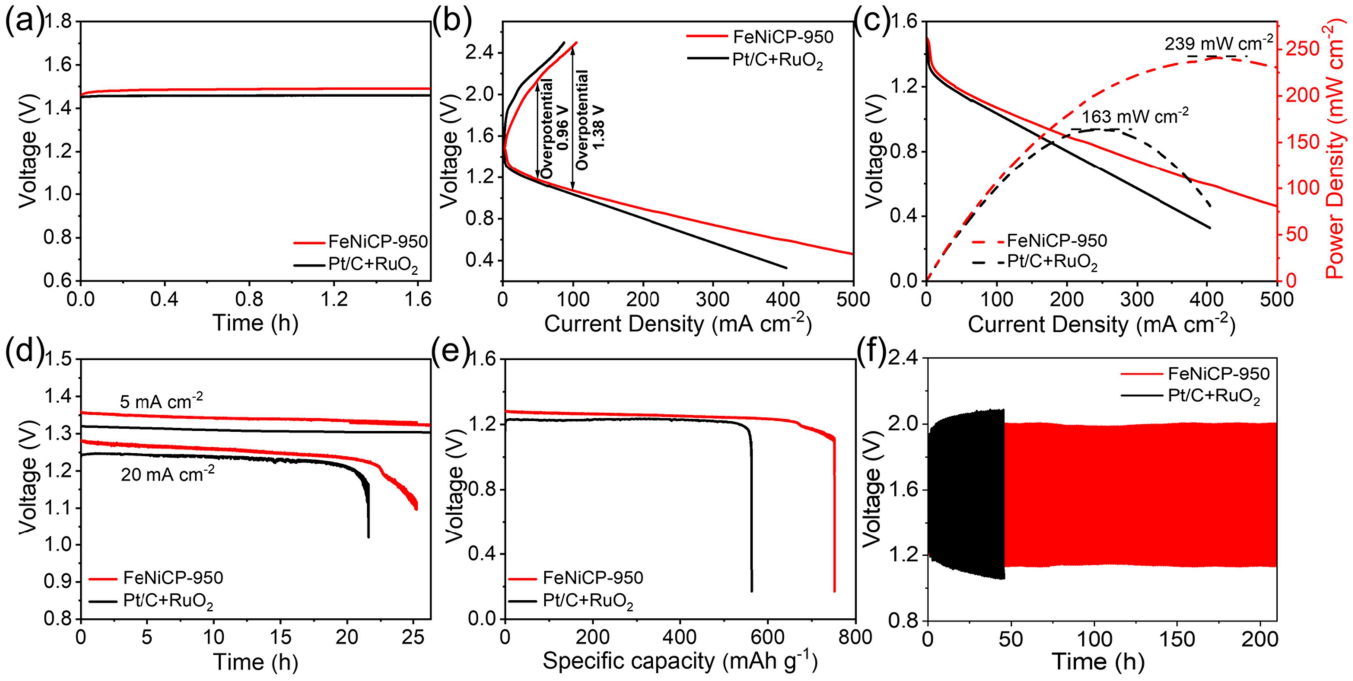

FIGURE 6 | (a) Open circuit potential diagrams, (b) charge/discharge voltage–current profiles, (c) power–density curves, (d) galvanostatic discharge curves at 5 mA cm^{-2} and 20 mA cm^{-2}, (e) specific capacity and (f) galvanostatic cyclic stability at 5 mA cm^{-2} of Zn-air battery with FeNiCP-950 and Pt/C + RuO_2 as catalysts.

of only 0.96 and 1.38 V under current intensities of 50 and 100 mA cm^{-2}, significantly outperforming the reference cell utilizing a conventional Pt/C + RuO_2 mixed electrocatalyst. Regarding power output (Figure 6c), the FeNiCP-950-based cell achieved the highest power density of 239 mW cm^{-2}, markedly outperforming the reference cell's value of 163 mAh cm^{-2}. Meanwhile, its discharge specific capacity reached 752 mAh g^{-1} (based on zinc consumption) (Figure 6e), which was also markedly higher than the 603 mAh g^{-1} of the control battery. More importantly, the battery exhibits outstanding cycling stability. During extended discharge tests at various current intensities, the voltage plateau remained stable (Figure 6d). Notably, in prolonged cycling experiments at 5 mA cm^{-2} (Figure 6f), after 210 h (630 cycles), the charge-discharge potential difference increased by only 0.09 V. In contrast, the reference battery exhibited significant deterioration, with its potential difference widening to 1.05 V from 0.71 V in just 45 h. This fully demonstrates that the FeNiCP-950 catalyst-driven zinc-air battery exhibits high power output, high energy density, and outstanding cycling durability. The detailed comparison of ORR, OER, and ZAB performance with recently reported FeNi-based bifunctional catalysts is summarized in Supporting Information S1: Tables S6–S9.

3 | Conclusions

In summary, this study successfully constructed a branched network porous carbon framework embedded with FeNi alloy species using ZnO as a structural template through a template-assisted assembly strategy [27]. During the pyrolysis process, ZnO serves as a structural-directing agent for carbon nanotubes and as a removable template for mesopore formation, thereby generating a high-surface-area conductive platform with putative ternary synergistic active sites (FeNi alloy/M-N_x) [79, 80]. This catalyst exhibits outstanding dual functionality for ORR/OER in an alkaline medium. The assembled zinc-air battery achieves synergistic enhancement of high-power density (239 mW cm^{-2}), elevated specific capacity (752 mAh g^{-1}), along with prolonged cycle life. This work provides a new strategy for designing advanced noble-metal-free electrocatalysts through template-guided assembly.

Acknowledgments

This work was supported by the Basic and Applied Basic Research Foundation of Guangdong Province (2024B1515130002), Foshan Xianhu Laboratory of the Advanced Energy Science and Technology Guangdong Laboratory (XHD2024-23000000-05, XHD2025-422501-01), National Natural Science Foundation of China (52506222), and the Fundamental Research Funds for the Central Universities (WUT. 104972025ZHZXhp0013).

Conflicts of Interest

The authors declare no conflicts of interest.

Data Availability Statement

The data that support the findings of this study are available from the corresponding author upon reasonable request.

References

1. P. Zhang, M. Wei, K. Wang, H. Wang, Y. Zuo, and M. Zhang, "Performance Optimization of Zinc-Air Batteries via Nanomaterials," *Energy Storage Materials* 75 (2025): 104109, https://doi.org/10.1016/j.ensm.2025.104109.

2. X. Li, J. Song, T. Tian, et al., "Lewis Acid-Base Molecular Anchoring Through Oxygen Vacancies Enables Ultrastable and High-Conductivity Membranes for Alkaline Water Electrolysis," *Advanced Energy Materials* 16 (2026): e06172, https://doi.org/10.1002/aenm.202506172.

3. H. Zhang, J. Xiao, Z. Meng, et al., "Harnessing Direct Oxo Coupling for Durable Water Oxidation via Atomic-Level Strain Engineering," *Advanced Materials* 38 (2026): e72241, https://doi.org/10.1002/adma.72241.

4. H. Li, L. Cui, F. Wu, et al., "Kinetically-Enhanced Gradient Modulator Layer Enables Wide-Temperature Ultralong-Life All-Solid-State Lithium-Sulfur Batteries," *Advanced Energy Materials* 15 (2025): 2501259, https://doi.org/10.1002/aenm.202501259.

5. F. Wu, H. Tang, J. Wang, et al., "Robust Interphase Derived From a Dual-Cation Ionic Liquid Electrolyte Enabling Exceptional Stability for Nickel-Rich Layered Cathodes," *Energy & Environmental Science* 18 (2025): 4740–4752, https://doi.org/10.1039/d5ee00669d.

6. H. Li, R. Wang, J. Song, et al., "In Situ-Constructed LiMoS With Highly Exposed Interface Boosting High-Loading and Long-Life Cathode for All-Solid-State Li-S Batteries," *Energy & Environmental Materials* 7 (2024): e12687, https://doi.org/10.1002/eem2.12687.

7. H. Li, J. Song, F. Wu, R. Wang, D. Liu, and H. Tang, "Metal-Nitrogen-Doped Hybrid Ionic/Electronic Conduction Triple-Phase Interfaces for High-Performance All-Solid-State Lithium-Sulfur Batteries," *Nano Research* 16 (2023): 10956–10965, https://doi.org/10.1007/s12274-023-5815-7.

8. Y. Li and H. Dai, "Recent Advances in Zinc-Air Batteries," *Chemical Society Reviews* 43 (2014): 5257–5275, https://doi.org/10.1039/c4cs00015c.

9. W. W. Zhang, Y. Wang, Y. C. Li, L. L. Sun, and X. Y. Zhang, "First-Principles Calculations Insight into Non-Noble-Metal Bifunctional Electrocatalysts for Zinc-Air Batteries," *Applied Energy* 391 (2025): 125925, https://doi.org/10.1016/j.apenergy.2025.125925.

10. P. Liu, Y. Wang, R. Lv, G. Zhang, X. Liu, and L. Wang, "Design Principles of Non-Noble Metal Catalysts for High-Performance Rechargeable Zn-Air Batteries," *Energy Storage Materials* 76 (2025): 104155, https://doi.org/10.1016/j.ensm.2025.104155.

11. R. B. Huang, M. Y. Wang, J. F. Xiong, H. Zhang, J. H. Tian, and J. F. Li, "Anode Optimization Strategies for Zinc-Air Batteries," *Escience* 5 (2025): 100309, https://doi.org/10.1016/j.esci.2024.100309.

12. M. Tamtaji, Y. Li, Y. Cai, H. Liu, W. A. Goddard, III, and G. Chen, "Reaction Mechanism and Kinetics of Oxygen Reduction Reaction on the Iron-Nickel Dual Atom Catalyst," *Journal of Materials Chemistry A* 11 (2023): 25410–25421, https://doi.org/10.1039/d3ta05694e.

13. X. F. Zhu, C. G. Hu, R. Amal, L. M. Dai, and X. Y. Lu, "Heteroatom-Doped Carbon Catalysts for Zinc-Air Batteries: Progress, Mechanism, and Opportunities," *Energy & Environmental Science* 13 (2020): 4536–4563, https://doi.org/10.1039/d0ee02800b.

14. J. C. Yan, Z. M. Tang, B. X. Li, D. Bi, Q. X. Lai, and Y. Y. Liang, "In Situ ZnO-Activated Hierarchical Porous Carbon Nanofibers as Self-Standing Electrodes for Flexible Zn-Air Batteries," *Acs Sustainable Chemistry & Engineering* 7 (2019): 17817–17824, https://doi.org/10.1021/acssuschemeng.9b04327.

15. P. Yu, L. Wang, F. Sun, et al., "Co Nanoislands Rooted on Co-N-C Nanosheets as Efficient Oxygen Electrocatalyst for Zn-Air Batteries," *Advanced Materials* 31 (2019): 1901666, https://doi.org/10.1002/adma.201901666.

16. F. Gu, W. Guo, Y. Yuan, et al., "External Field-Responsive Ternary Non-Noble Metal Oxygen Electrocatalyst for Rechargeable Zinc-Air Batteries," *Advanced Materials* 36 (2024): e2313096, https://doi.org/10.1002/adma.202313096.

17. Y. Gao, L. Liu, Y. Jiang, et al., "Design Principles and Mechanistic Understandings of Non-Noble-Metal Bifunctional Electrocatalysts for Zinc-Air Batteries," *Nano-Micro Letters* 16 (2024): 162, https://doi.org/10.1007/s40820-024-01366-9.

18. H. Wang, C. Tang, and Q. Zhang, "A Review of Precious-Metal-Free Bifunctional Oxygen Electrocatalysts: Rational Design and Applications in Zn-Air Batteries," *Advanced Functional Materials* 28 (2018): 1803329, https://doi.org/10.1002/adfm.201803329.

19. Z. Xu, W. Chen, G. Liu, et al., "Bamboo-Like Carbon Nanotubes and N-Doped Porous Carbon Nanosheets-Encapsulated Co/Co7Fe3 Interfacial Nanoparticles as Bifunctional Oxygen Electrocatalysts for Rechargeable Zinc-Air Batteries," *Chemical Engineering Journal* 515 (2025): 163536, https://doi.org/10.1016/j.cej.2025.163536.

20. S. Zha, D. Wang, X. Li, et al., "Coupling of Fe-Nx Sites and Fe Nanoparticles on Nitrogen-Doped Porous Carbon for Boosting Oxygen Electroreduction in Zn-Air Batteries," *Journal of Energy Storage* 96 (2024): 112672, https://doi.org/10.1016/j.est.2024.112672.

21. Y. J. Li, L. Cui, P. F. Da, et al., "Multiscale Structural Engineering of Ni-Doped CoO Nanosheets for Zinc-Air Batteries With High Power Density," *Advanced Materials* 30 (2018): e1804653, https://doi.org/10.1002/adma.201804653.

22. L. Gao, X. Zhong, Z. Li, et al., "A Multi-Layer Reduced Graphene Oxide Catalyst Encapsulating a High-Entropy Alloy for Rechargeable Zinc-Air Batteries," *Chemical Communications* 60 (2024): 1269–1272, https://doi.org/10.1039/d3cc05069f.

23. A. Xie, X. Tai, Y. Guo, et al., "Elaborate Construction of Honeycomb-Like Porous Carbon With Embedment of N-Doped Carbon Nanotubes as Efficient Electrocatalyst for Zinc-Air Battery," *Carbon* 228 (2024): 119299, https://doi.org/10.1016/j.carbon.2024.119299.

24. Y. Guo, Y. N. Chen, H. Cui, and Z. Zhou, "Bifunctional Electrocatalysts for Rechargeable Zn-Air Batteries," *Chinese Journal of Catalysis* 40 (2019): 1298–1310, https://doi.org/10.1016/S1872-2067(19)63349-8.

25. R. Luo, R. Wang, Y. Cheng, et al., "Yttrium Oxide Nanoclusters Boosted Fe-N4 and Fe4N Electrocatalyst for Future Zinc–Air Battery," *Advanced Functional Materials* 34 (2024): 2311084, https://doi.org/10.1002/adfm.202311084.

26. Y. Xia, Y. Cheng, R. Wang, et al., "Porous Nanosheet Composite With Multi-Type Active Centers as An Efficient and Stable Oxygen Electrocatalyst in Alkaline and Acid Conditions," *Science China Materials* 66 (2022): 1407–1416, https://doi.org/10.1007/s40843-022-2272-2.

27. C. Zhu, S. Fu, J. Song, et al., "Self-Assembled Fe-N-Doped Carbon Nanotube Aerogels With Single-Atom Catalyst Feature as High-Efficiency Oxygen Reduction Electrocatalysts," *Small* 13 (2017): 1603407, https://doi.org/10.1002/smll.201603407.

28. X. Wang, D. Wu, S. Liu, J. Zhang, X. Z. Fu, and J. L. Luo, "Folic Acid Self-Assembly Enabling Manganese Single-Atom Electrocatalyst for Selective Nitrogen Reduction to Ammonia," *Nano-Micro Letters* 13 (2021): 125, https://doi.org/10.1007/s40820-021-00651-1.

29. X. Wang, J. Sun, T. Li, et al., "Folic Acid Self-Assembly Synthesis of Ultrathin N-Doped Carbon Nanosheets With Single-Atom Metal Catalysts," *Energy Storage Materials* 36 (2021): 409–416, https://doi.org/10.1016/j.ensm.2021.01.024.

30. J. Xu, Y. Meng, X. Qiu, et al., "Honeycomb-Like Single-Atom Catalysts With FeN3Cl Sites for High-Performance Oxygen Reduction," *Advanced Powder Materials* 4 (2025): 100298, https://doi.org/10.1016/j.apmate.2025.100298.

31. H. Xu, D. Wang, P. Yang, et al., "A Hierarchically Porous Fe-Nc Synthesized by Dual Melt-Salt-Mediated Template as Advanced Electrocatalyst for Efficient Oxygen Reduction in Zinc-Air Battery," *Applied Catalysis, B: Environmental* 305 (2022): 121040, https://doi.org/10.1016/j.apcatb.2021.121040.

32. Y. Chen, S. Zhang, J. Chung-Yen jung, and J. Zhang, "Carbons as Low-Platinum Catalyst Supports and Non-Noble Catalysts for Polymer Electrolyte Fuel Cells," *Progress in Energy and Combustion Science* 98 (2023): 101101, https://doi.org/10.1016/j.pecs.2023.101101.

33. J. Kim, G. Y. Kim, J. S. Lim, J. Woo, H. Y. Kim, and S. H. Joo, "Recent Advances in Mesostructured Electrocatalysts for Energy Conversion Reactions," *Chemistry of Materials* 38 (2026): 2156–2183, https://doi.org/10.1021/acs.chemmater.5c03206.

34. J. Tang, Q. Zhang, Y. Liu, et al., "The Photocatalytic Redox Properties of Polymeric Carbon Nitride Nanocages (PCNCs) With Mesoporous Hollow Spherical Structures Prepared by a ZnO-Template Method," *Microporous and Mesoporous Materials* 292 (2020): 109639, https://doi.org/10.1016/j.micromeso.2019.109639.

35. Y. Yoon, S. Choi, J. Park, H. Baek, J. Jeon, and T. Lim, "ZnO-Templated Ni-Based Bifunctional Catalyst for Efficient Anion Exchange Membrane Water Electrolysis," *Journal of the American Ceramic Society* 108 (2025): e20653, https://doi.org/10.1111/jace.20653.

36. S. Saha, S. Mitra, Y. P. Kharwar, H. V. Annadata, S. Roy, and A. Dutta, "A Molecular Catalyst-Driven Sustainable Zinc-Air Battery Assembly," *Small* 21 (2025): e2411021, https://doi.org/10.1002/smll.202411021.

37. L. Peng, H. Peng, Y. Yuan, et al., "Nanoemulsion Modular Assembly for the Synthesis of Functional Mesoporous Nanomaterials," *Nature Synthesis* 5 (2026): 162–179, https://doi.org/10.1038/s44160-025-00973-7.

38. J. Meng, J. Li, J. Liu, et al., "Universal Approach to Fabricating Graphene-Supported Single-Atom Catalysts From Doped ZnO Solid Solutions," *ACS Central Science* 6 (2020): 1431–1440, https://doi.org/10.1021/acscentsci.0c00458.

39. S. Di, C. Guo, Y. Dai, F. Wang, Z. Wang, and H. Zhu, "Nitrogen-Doped Porous Carbon-Supported PtCo Nanoparticle Electrocatalyst for Oxygen Reduction Reaction Prepared by a Dual-Template Method," *ACS Applied Energy Materials* 6 (2023): 1639–1649, https://doi.org/10.1021/acsaem.2c03543.

40. R. Anne Acedera, A. Theresse Dumlao, D. Donn Matienzo, et al., "Templated Synthesis of Transition Metal Phosphide Electrocatalysts for Oxygen and Hydrogen Evolution Reactions," *Journal of Energy Chemistry* 89 (2024): 646–669, https://doi.org/10.1016/j.jechem.2023.10.044.

41. C. Lin, S. S. Shinde, Z. Jiang, et al., "In Situ Directional Formation of Co@CoOx-Embedded 1D Carbon Nanotubes as An Efficient Oxygen Electrocatalyst for Ultra-High Rate Zn–Air Batteries," *Journal of Materials Chemistry A* 5 (2017): 13994–14002, https://doi.org/10.1039/c7ta02215h.

42. P. C. Shi, J. D. Yi, T. T. Liu, et al., "Hierarchically Porous Nitrogen-Doped Carbon Nanotubes Derived From Core–Shell ZnO@Zeolitic Imidazolate Framework Nanorods for Highly Efficient Oxygen Reduction Reactions," *Journal of Materials Chemistry A* 5 (2017): 12322–12329, https://doi.org/10.1039/c7ta02999c.

43. Y. Pan, K. Sun, S. Liu, et al., "Core-Shell ZIF-8@ZIF-67-Derived CoP Nanoparticle-Embedded N-Doped Carbon Nanotube Hollow Polyhedron for Efficient Overall Water Splitting," *Journal of the American Chemical Society* 140 (2018): 2610–2618, https://doi.org/10.1021/jacs.7b12420.

44. R. Baker, "Nucleation and Growth of Carbon Deposits From the Nickel Catalyzed Decomposition of Acetylene," *Journal of Catalysis* 26 (1972): 51–62, https://doi.org/10.1016/0021-9517(72)90032-2.

45. R. Baker, "Formation of Filamentous Carbon From Iron, Cobalt and Chromium Catalyzed Decomposition of Acetylene," *Journal of Catalysis* 30 (1973): 86–95, https://doi.org/10.1016/0021-9517(73)90055-9.

46. W. H. Chiang and R. M. Sankaran, "Synergistic Effects in Bimetallic Nanoparticles for Low Temperature Carbon Nanotube Growth," *Advanced Materials* 20 (2008): 4857–4861, https://doi.org/10.1002/adma.200801006.

47. N. Gupta, S. M. Gupta, and S. K. Sharma, "Carbon Nanotubes: Synthesis, Properties and Engineering Applications," *Carbon Letters* 29 (2019): 419–447, https://doi.org/10.1007/s42823-019-00068-2.

48. J. Sheng, Y. Xu, Z. Han, et al., "Catalytic Joule Heating Synthesis of One-Dimensional Nanomaterials in Seconds," *Nature Synthesis* 5 (2025): 367–376, https://doi.org/10.1038/s44160-025-00933-1.

49. Z. Li, M. Hou, M. Chen, et al., "Engineering SmPO4-integrated N, P-Doped Porous Carbon Nanosheets for Enhanced Oxygen Reduction in Zinc-Air Batteries," *Journal of Colloid and Interface Science* 697 (2025): 137921, https://doi.org/10.1016/j.jcis.2025.137921.

50. H. Liu, S. Shi, Z. Wang, Y. Han, and W. Huang, "Recent Advances in Metal-Gas Batteries With Carbon-Based Nonprecious Metal Catalysts," *Small* 18 (2022): e2103747, https://doi.org/10.1002/smll.202103747.

51. H. M. Xu, C. J. Huang, T. Y. Shuai, et al., "Noble Metal-Free N-Doped Carbon-Based Electrocatalysts for Air Electrode of Rechargeable Zinc-Air Battery," *Science China Materials* 66 (2023): 2953–3003, https://doi.org/10.1007/s40843-023-2464-8.

52. K. Yu, J. Qin, H. Zhang, et al., "Tailoring the First/Second Coordination Layer of FeNi Single Atoms With Nucleophile Atoms to Boost Oxygen Electrocatalysis for Zinc-Air Batteries," *Advanced Energy Materials* 15 (2025): 2501091, https://doi.org/10.1002/aenm.202501091.

53. S. Sandoval, G. Gonçalves, J. Pérez Barrio, M. V. Kharlamova, and G. Tobías-Rossell, "A Comprehensive Review on Filled Carbon Nanotubes: Synthesis, Properties and Applications," *Chemical Reviews* 126 (2026): 2283–2390, https://doi.org/10.1021/acs.chemrev.5c00219.

54. Y. Chen, I. Kone, Y. Gong, et al., "Ultra-Thin Carbon Nanosheets-Assembled 3D Hierarchically Porous Carbon for High Performance Zinc-Air Batteries," *Carbon* 152 (2019): 325–334, https://doi.org/10.1016/j.carbon.2019.06.026.

55. J. Choi, H. Jang, J. Park, et al., "Progress and Challenges in Engineering the Atomic Structure of Oxygen Electrocatalysts for Zinc-Air Batteries," *Chemical Engineering Journal* 497 (2024): 154561, https://doi.org/10.1016/j.cej.2024.154561.

56. S. Sakurai, H. Nishino, D. N. Futaba, et al., "Role of Subsurface Diffusion and Ostwald Ripening in Catalyst Formation for Single-Walled Carbon Nanotube Forest Growth," *Journal of the American Chemical Society* 134 (2012): 2148–2153, https://doi.org/10.1021/ja208706c.

57. D. Chen, J. Zhu, X. Mu, et al., "Nitrogen-Doped Carbon Coupled FeNi3 Intermetallic Compound as Advanced Bifunctional Electrocatalyst for Oer, Orr and Zn-Air Batteries," *Applied Catalysis B: Environment and Energy* 268 (2020): 118729, https://doi.org/10.1016/j.apcatb.2020.118729.

58. M. Hayase, M. Shiga, and Y. Nakamura, "Spontaneous Volume Magnetostriction and Lattice Constant of Face-Centered Cubic Fe-Ni and Ni-Cu Alloys," *Journal of the Physical Society of Japan* 34 (1973): 925–933, https://doi.org/10.1143/jpsj.34.925.

59. D. Olekšáková, J. Füzer, P. Kollár, J. Bednarčík, and C. Lathe, "Isobaric Thermal Expansion and Isothermal Compression of Powdered NiFe Based Alloys Studied by In-Situ EDXRD," *Acta Physica Polonica A* 126 (2014): 128–129, https://doi.org/10.12693/APhysPolA.126.128.

60. M. A. R. Martinez, F. F. H. Aragón, L. L. Félix, et al., "Phase Stability and Tunable Structural, Hyperfine, and Magnetic Properties of Sol-Gel FeNi Nanoparticles," *Journal of Magnetism and Magnetic Materials* 640 (2026): 173792, https://doi.org/10.1016/j.jmmm.2025.173792.

61. R. Wu, X. Wang, L. Ge, et al., "N, S Co-Doped Carbon With Embedment of Feni Alloy as Bifunctional Oxygen Electrocatalysts for Rechargeable Zinc-Air Batteries," *Carbon* 202 (2023): 141–149, https://doi.org/10.1016/j.carbon.2022.10.047.

62. S. Liu, K. Dong, X. Lei, et al., "FeNi Alloy Embedded in Three-Dimensional Nitrogen-Doped Porous Carbon as Bifunctional Oxygen Electrocatalysts for Rechargeable Zn-Air Batteries," *Journal of Energy Storage* 89 (2024): 111862, https://doi.org/10.1016/j.est.2024.111862.

63. M. Zhang, X. Hu, Y. Xin, et al., "Feni Coordination Polymer Based Highly Efficient and Durable Bifunction Oxygen Electrocatalyst for Rechargeable Zinc-Air Battery," *Separation and Purification Technology* 308 (2023): 122974, https://doi.org/10.1016/j.seppur.2022.122974.

64. D. Zhu, Y. Huang, X. Shi, et al., "Enhancing Molecular Oxygen Activation by Nitrogen-Doped Carbon Encapsulating Feni Alloys With Ultra-Low Pt Loading," *PNAS Nexus* 4 (2025): pgae594, https://doi.org/10.1093/pnasnexus/pgae594.

65. Y. Guo, Y. Xue, and Z. Zhou, "Revolutionizing Zn-Air Batteries With Chainmail Catalysts: Ultrathin Carbon-Encapsulated Feni Alloys on N-Doped Graphene for Enhanced Oxygen Electrocatalysis," *Chinese Journal of Catalysis* 58 (2024): 206–215, https://doi.org/10.1016/S1872-2067(23)64603-0.

66. S. Wang, M. Zhang, X. Mu, S. Liu, D. Wang, and Z. Dai, "Atomically Dispersed Multi-Site Catalysts: Bifunctional Oxygen Electrocatalysts Boost Flexible Zinc–Air Battery Performance," *Energy & Environmental Science* 17 (2024): 4847–4870, https://doi.org/10.1039/D4EE01656D.

67. B. Yang, W. Liu, T. Gu, and Z. Wu, "Material Design and Catalyst-Membrane Electrode Interface Engineering for High-Performance Rechargeable Zinc-Air Batteries," *Energy Storage Materials* 74 (2025): 103985, https://doi.org/10.1016/j.ensm.2024.103985.

68. S. Liu, I. S. Amiinu, X. Liu, et al., "Carbon Nanotubes Intercalated Co/N-Doped Porous Carbon Nanosheets as Efficient Electrocatalyst for Oxygen Reduction Reaction and Zinc-Air Batteries," *Chemical Engineering Journal* 342 (2018): 163–170, https://doi.org/10.1016/j.cej.2018.02.039.

69. X. Zheng, X. Cao, K. Zeng, et al., "A Self-Jet Vapor-Phase Growth of 3D FeNi@ Ncnt Clusters as Efficient Oxygen Electrocatalysts for Zinc-Air Batteries," *Small* 17 (2021): 2006183, https://doi.org/10.1002/smll.202006183.

70. C. Liang, T. Zhang, S. Sun, et al., "Yolk–Shell FeCu/NC Electrocatalyst Boosting High-Performance Zinc-Air Battery," *Nano Research* 17 (2024): 7918–7925, https://doi.org/10.1007/s12274-024-6766-3.

71. H. Liu, F. Yu, K. Wu, et al., "Recent Progress on Fe-Based Single/Dual-Atom Catalysts for Zn–Air Batteries," *Small* 18 (2022): 2106635, https://doi.org/10.1016/j.nanoms.2024.09.008.

72. Y. Cheng, Y. Zhang, W. Guan, et al., "Axial Coordination Engineering of FeNi Catalysts for Oxygen Evolution Reaction," *Journal of Colloid and Interface Science* 698 (2025): 138096, https://doi.org/10.1016/j.jcis.2025.138096.

73. J. Chen, L. Li, Y. Cheng, Y. Huang, and C. Chen, "Covalent Organic Polymer Derived N–Doped Carbon Confined Feni Alloys as Bifunctional Oxygen Electrocatalyst for Rechargeable Zinc-Air Battery," *International Journal of Hydrogen Energy* 47 (2022): 16025–16035, https://doi.org/10.1016/j.ijhydene.2022.03.100.

74. Y. Zhou, Y. Li, L. Zhang, et al., "Fe-Leaching Induced Surface Reconstruction of Ni-Fe Alloy on N-Doped Carbon to Boost Oxygen Evolution Reaction," *Chemical Engineering Journal* 394 (2020): 124977, https://doi.org/10.1016/j.cej.2020.124977.

75. G. Zhang, J. Zeng, J. Yin, et al., "Iron-Facilitated Surface Reconstruction to In-Situ Generate Nickel–Iron Oxyhydroxide on Self-Supported Feni Alloy Fiber Paper for Efficient Oxygen Evolution Reaction," *Applied Catalysis, B: Environmental* 286 (2021): 119902, https://doi.org/10.1016/j.apcatb.2021.119902.

76. M. Pascuzzi, A. Man, A. Goryachev, J. Hofmann, and E. Hensen, "Investigation of the Stability of NiFe-(Oxy)Hydroxide Anodes in Alkaline Water Electrolysis under Industrially Relevant Conditions," *Catalysis Science & Technology* 10 (2020): 5593–5601, https://doi.org/10.1039/d0cy01179g.

77. G. Helal, Z. Xu, W. Zuo, J. Qian, G. Cheng, and P. Zhao, "Nitrogen-Induced Deep Reconstruction and Formation of a High-Valent Nickel Species γ-NiOOH Surface Layer on NiFealloy/NiFeN Pre-Catalysts for Efficient Water Oxidation," *Journal of Materials Chemistry A* 13 (2025): 13440–13456, https://doi.org/10.1039/d4ta09149c.

78. S. Zhang, L. Yang, T. Yang, et al., "Pomegranate-Like Structured FeNi-Nanodots@ Feni LDH Composite as a High Performance Bifunctional Catalyst for Oxygen Electrocatalytic Reactions in Zinc-Air Batteries," *Composites Communications* 44 (2023): 101757, https://doi.org/10.1016/j.coco.2023.101757.

79. M. Wang, Y. Wang, S. S. Mao, and S. Shen, "Transition-Metal Alloy Electrocatalysts With Active Sites Modulated by Metal-Carbide Heterophases for Efficient Oxygen Evolution," *Nano Energy* 88 (2021): 106216, https://doi.org/10.1016/j.nanoen.2021.106216.

80. Z. Zheng, F. Zheng, B. Huang, et al., "An Open Decoupled Cell Design Achieving Electricity Generation and Amplification Through Waste-To-Energy Conversion," *Nature Communications* 17 (2026): 1838, https://doi.org/10.1038/s41467-026-68550-w.

Supporting Information

Additional supporting information can be found online in the Supporting Information section.

Supporting File 1: bte270119-sup-0001-Supplementary_Material.docx.